Journal of Materials Chemistry A

Unconventional charge compensation mechanism for proton insertion in aqueous Zn-ion batteries

Journal:	*Journal of Materials Chemistry A*
Manuscript ID	TA-ART-07-2024-005214.R1
Article Type:	Paper
Date Submitted by the Author:	27-Sep-2024

Complete List of Authors:	Wang, Jiwei; Binghamton University Huang, Heran; Binghamton University, Department of Chemistry Qiao, Linna; Binghamton University Wang, Haonan; Binghamton University Lee, Krystal; Binghamton University Harpur College of Arts and Sciences, Chemistry Zhou, Guangwen; Binghamton University, Mechanical Engineering Liu, Hao; Binghamton University, Department of Chemistry

ARTICLE

Unconventional Charge Compensation Mechanism for Proton Insertion in Aqueous Zn-Ion Batteries

Received 00th January 20xx,
Accepted 00th January 20xx

DOI: 10.1039/x0xx00000x

Jiwei Wang,[a] Heran Huang,[b] Linna Qiao,[b] Haonan Wang,[b] Krystal Lee,[a] Guangwen Zhou,[b,c] Hao Liu[a,b]*

Aqueous Zn-ion batteries have been proposed as safe and economical options for large-scale energy storage. In theory, they operate by reversibly shuttling zinc ions between a metallic zinc anode and a cathode material for Zn^{2+} ion intercalation through an aqueous electrolyte of a zinc salt solution. In practice, protons (H^+) in the aqueous electrolyte can compete with and even predominate Zn^{2+} in the intercalation reaction. A diagnostic consequence of H^+, as opposed to Zn^{2+}, insertion is the precipitation of layered double hydroxide (LDH) crystals, which can be readily identified by electron microscopy and X-ray diffraction measurements. Absence of LDH formation has been perceived as evidence for Zn^{2+} insertion. Using a combination of X-ray diffraction, electron microscopy, X-ray photoelectron spectroscopy, we reveal a different charge compensation mechanism in a vanadyl phosphate electrode, where H^+ insertion predominates in an aqueous $Zn(CF_3SO_3)_2$ electrolyte. The H^+ insertion induces a conformal deposition of an amorphous ZnO layer on the electrode particle, which cannot be captured by scanning electron microscopy or X-ray diffraction. Our work underlines the complexity of the charge compensation mechanism in aqueous Zn-ion batteries, which is relevant to other multivalent systems.

1. Introduction

In the pursuit of sustainable energy solutions, aqueous Zn-ion batteries (AZIBs) have emerged as promising candidates due to their high safety, low cost, and abundance of zinc resources.[1, 2] Despite these inherent advantages, AZIBs face a formidable challenge – the scarcity of robust cathode materials. Several manganese- and vanadium-based intercalation compounds have been proposed as cathode materials for AZIBs with promising electrochemical performance.[3-5] However, ambiguity surrounds the charge storage mechanism regarding whether the reaction involves reversible Zn^{2+} intercalation. In particular, H^+ in the aqueous electrolyte presents a competing, if not the dominant, species for the intercalation reaction. For example, a recent electron microscopic study shows H^+ as the predominant intercalating ion for α-MnO_2 in an aqueous Zn electrolyte.[6] This undesired H^+ (co)insertion typically induces the precipitation of the layered double hydroxide (LDH) due to changes in the local pH of the electrolyte.[7, 8] Thus, the formation of the LDH during the cycling of AZIBs is considered evidence for proton (co)insertion. Interestingly, LDH is typically observed in the cycling of oxide-based materials but not sulfides, suggesting favorable Zn^{2+} intercalation in non-oxide cathodes.[7] Engineering the aqueous Zn electrolyte also suppresses the LDH formation[9, 10] and offers a possible pathway to promote Zn^{2+} insertion.

Notwithstanding the progress with the understanding of the charge storage mechanism in AZIBs, direct structural evidence for Zn-ion intercalation remains elusive. Given its high atomic number, the intercalated Zn ions should be readily captured in the real space by imaging techniques (e.g., high-resolution transmission electron microscopy) or in the reciprocal space by scattering techniques (e.g., X-ray diffraction). Yet, most studies only report changes in the lattice parameters or elemental mapping of Zn without explicit determination of the position and occupation of the intercalation site for Zn^{2+} ions. To the best of our knowledge, the Zn-intercalated crystal structure has only been reported for a handful of vanadium phosphate-based cathode materials through the Rietveld analysis.[9, 11, 12] The lack of direct structural evidence brings into question the use of indirect methods (e.g., observation of LDH formation) for validating Zn ion intercalation and undermines the understanding of the complex charge storage mechanism in AZIBs. Therefore, it is imperative to use direct structural probes to interrogate the intercalated electrodes in AZIBs.

Among various cathode materials, vanadium-based compounds (vanadium-based oxides and phosphates) have attracted much interest owing to their exceptional electrochemical properties, such as high theoretical capacity and high operating voltage.[13] While proton (co)insertion is a common occurrence in vanadium oxide and VPO_4F cathodes,[14, 15] little is known about the actual charge storage mechanism in $VOPO_4$ cathodes, which have demonstrated promising electrochemical performance for its various polymorphs.[16-19] Specifically, the oversight of the structural analysis of the intercalated phase raises doubt on the veracity of Zn ion intercalation in $VOPO_4$.

[a] Department of Chemistry, Binghamton University, Binghamton, New York 13902, United States
[b] Materials Science and Engineering, Binghamton University, Binghamton, New York 13902, United States
[c] Department of Mechanical Engineering, Binghamton University, Binghamton, New York 13902, United States

† Footnotes relating to the title and/or authors should appear here.
Supplementary Information available: [details of any supplementary information available should be included here]. See DOI: 10.1039/x0xx00000x

Here, we employed ε-$VOPO_4$ as a model compound to investigate the intercalation mechanism in an aqueous $Zn(CF_3SO_3)_2$ electrolyte. Structural analysis of the operando synchrotron X-ray diffraction (XRD) and high-resolution XRD results unequivocally show the absence of Zn in the intercalated phase, which exclusively contains proton. Remarkably, the predominant proton insertion does not induce the precipitation of any LDH phase. Instead, a thin Zn-based layer on the ε-$VOPO_4$ particle surface is revealed by transmission electron microscopy (TEM). This work uncovers a new charge compensation mechanism for proton insertion and underlines structural analysis in revealing complex reaction mechanisms in AZIBs.

2. Results and discussion

2.1 Characterization of as-synthesized ε-$VOPO_4$

All diffraction peaks of the as-synthesized ε-$VOPO_4$ sample can be indexed to Space Group *Cc* adopted by the ε-$VOPO_4$ polymorph (**Figure 1A**)[20], whose crystal structure is shown in **Figure 1B**. The refined unit cell parameters are a = 7.2656(6) Å, b = 6.88178(1) Å, c = 7.2611(6) Å, and β = 115.3400(1)°, which are in good agreement with the previously reported values.[21] The ε-$VOPO_4$ particles exhibit a cuboid morphology with primary particle sizes in the range of 100 to 200 nm (**Figure S1**), consistent with the morphology reported by Chen et al. using the same synthesis method.[22] STEM EDS elemental mapping demonstrates the uniform distribution of V, P, and O elements throughout a single $VOPO_4$ particle (**Figure 1C**).

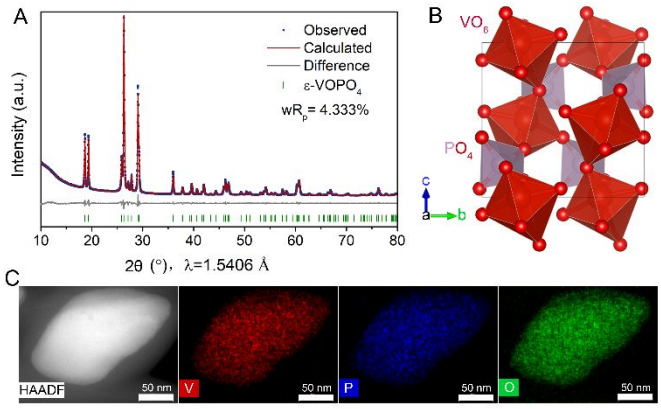

Figure 1. (A) XRD pattern with Rietveld refinement; (B) structure model of ε-$VOPO_4$ projected in b-c plane; and (C) HAADF image of an as-synthesized ε-$VOPO_4$ particle along with the elemental mapping of V (red), P (blue), and O (green).

2.2 Electrochemical performance of ε-$VOPO_4$

Galvanostatic charge-discharge was performed to investigate the intercalation chemistry of as-synthesized ε-$VOPO_4$ in aqueous Zn ion electrolytes. Swagelok-type cells were employed for the measurement with a zinc foil as the anode and a 3M $Zn(CF_3SO_3)_2$ aqueous solution as the electrolyte. **Figure 2A** displays the initial galvanostatic discharge and charge profile of the ε-$VOPO_4$ cathode cycled at a current rate of C/50 (3.3 mA/g). The discharge process shows two distinct voltage plateaus at 1.4 V and 1.25 V, which are apparent as peaks in the differential capacity plot in **Figure 2B**. The discharge capacity is 119 mAh/g, corresponding to the transfer of 0.72 electrons per formula unit (f.u.) of $VOPO_4$. This discharge capacity is comparable with previously reported values for vanadium phosphate-based type cathodes ($LiV_2(PO_4)_3$, δ-$VOPO_4$, $Na_3V_2(PO_4)_3$) in AZIBs.[11, 16, 23, 24] The charge process also exhibits two voltage plateaus at 1.4 V and 1.55 V, mirroring the discharge process. This suggests a reversible reaction during discharge and charge. The appearance of two distinct voltage plateaus seems to imply the presence of multiple phase transitions or reaction mechanisms. For example, the two distinct voltage plateaus observed for VPO_4F in AZIBs have been attributed to the sequential Zn ion and proton intercalation.[9] However, only a single phase transition is identified during the discharge process through structural characterization, which is described in the next section. The voltage profile changes into a sloping curve with increasing cycle number (**Figure S2**), which suggests the instability of ε-$VOPO_4$ in aqueous environments (**Figure S3**).

2.3 Reaction mechanism during the first cycle

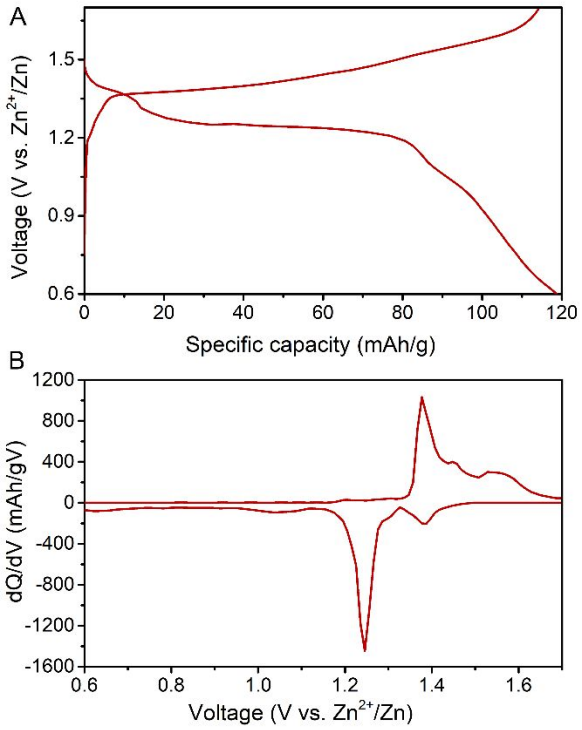

Figure 2. (A) Voltage profile of the galvanostatic cycling of the ε-$VOPO_4$ cathode cycled at C/50 between 0.6 V and 1.7V, and (B) the corresponding differential capacity (dQ/dV) curve highlighting the voltage plateaus.

To elucidate the structural evolution of ε-$VOPO_4$ during discharge and charge in the first cycle, *ex situ* XRD was measured for the pristine electrode, the electrode discharged to 0.6 V, and the electrode charged to 1.7 V following an initial discharge to 0.6 V (**Figure 3A**). For the electrode discharged to 0.6 V, a set of new Bragg peaks emerges together with significant intensity variations for peaks assigned to ε-$VOPO_4$ (indicated by asterisks in **Figure 3A**), which indicates substantial structural changes of the ε-$VOPO_4$ phase as a result of this initial discharge reaction. The preservation of sharp Bragg peaks during the first discharge suggests a topotactical structural evolution, which is characteristic of the intercalation reaction,

as opposed to the conversion reaction that typically results in the loss of sharp Bragg peaks. Upon charging back to 1.7 V, the electrode shows an XRD pattern similar to the pristine electrode, indicating a reversible reaction in the first cycle. Complementary XAS measurement was performed for the pristine, discharged, and charged electrodes to track changes of the V oxidation state during the first cycle (**Figure 3B**). The pristine electrode shows a main edge at 5488.2 eV and a pre-edge peak at 5470.7 eV, which agrees well with the K-edge spectra for $VOPO_4$.[25, 26] The pre-edge corresponds to the transition from 1s to 3d unoccupied orbitals and is sensitive to the local electronic structure around the absorbing atom.[27] For the electrode discharged to 0.6 V, the main edge shifted toward a lower energy, accompanied by the appearance of a pre-edge peak characteristic of V^{4+} at 5469.3 eV. This demonstrates the reduction of V^{5+} to V^{4+} during the first discharge. When the electrode charges back to 1.7 V, the main edge shifts back to its original position as observed for $VOPO_4$, which corresponds to the oxidation of V^{4+} back to V^{5+}. This XAS result shows the reversible redox of V^{5+}/V^{4+} during the first discharge and charge cycle, consistent with the reversible structural changes observed in the *ex situ* XRD result.

To unravel the reaction mechanism during the first cycle, we analyzed the crystal structure of the electrode discharged to 0.6 V. Following an initial failed attempt to index all Bragg peaks observed for the electrode discharged to 0.6 V with a single phase, we fitted the XRD pattern with an ε-$VOPO_4$ phase and individual peaks assigned to an unidentified phase to model the XRD pattern as a two-phase mixture. Indexing only the peaks assigned to the unidentified phase successfully yielded a unit cell in Space Group (S.G.) *Cc*, which is also adopted by ε-$VOPO_4$. The unit cell volume (335.14 ± 0.01 Å^3) of the newly indexed phase is only 1.8 % larger than ε-$VOPO_4$ (328.88 Å^3),[21] which suggests a topotactic transformation between ε-$VOPO_4$ and this new phase, likely induced by ion intercalation. Hence, Rietveld refinement was attempted to determine the structure of this intercalated phase using the structure parameters of ε-$VOPO_4$[21] as the initial structure model. The refinement resulted in a satisfactory fitting profile (**Figure 4A**) and a reasonably refined structure model (**Table S1**) even without considering any intercalated species. The average V-O bond length in the new phase is significantly longer than in ε-$VOPO_4$, which is consistent with the reduction of V^{5+}. The refined molar phase fraction of the intercalated phase is 63.0 ± 0.2 %, which is in good agreement with the fraction of V^{4+} species estimated from the discharge capacity of this electrode (**Figure S4**). This suggests that V in the intercalated phase assumes +4 oxidation state. The refined cell volume and the average V-O bond length are intermediate between $VOPO_4$ and H_2VOPO_4[28] (**Figure 4B**), which is consistent with the assignment of +4 for V in the intercalated phase. The failure to observe any intercalated species through XRD indicates proton, not Zn^{2+}, insertion as the charge compensation mechanism for the observed reduction of V ions during discharge. While it is impossible to refine the position and occupancy of protons against XRD data, charge balance assuming V^{4+} suggests a chemical formula of $HVOPO_4$ for the intercalated phase. Hereafter, $HVOPO_4$ is used to denote the intercalated phase.

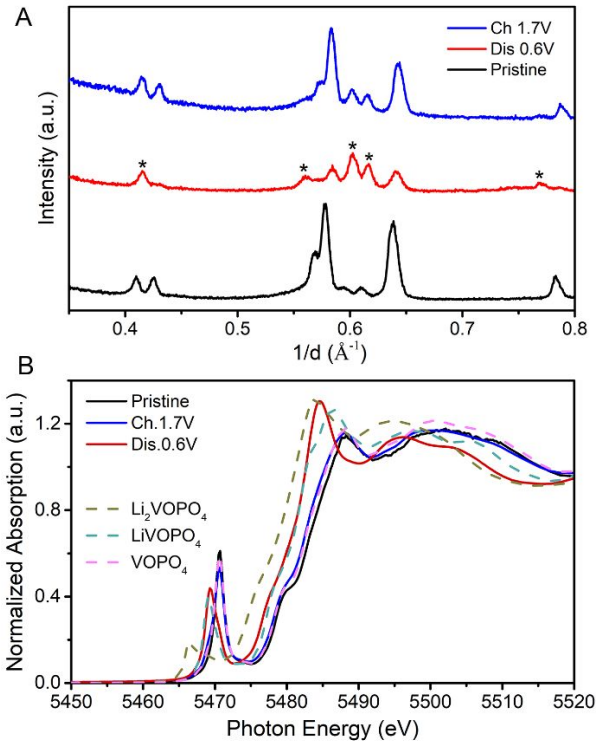

Figure 3. (A) Ex situ X-ray diffraction patterns and(B) V K-edge X-ray absorption near edge structure (XANES) spectra measured for the pristine electrode, the electrode at the end of first discharge at 0.6 V (Dis 0.6 V), and the electrode at the end of first charge at 1.7 V following an initial discharge to 0.6 V (Ch 1.7 V). Asterisks indicate Bragg peaks not observed in the ε-VOPO4 phase or those whose intensity varies significantly from the pristine ε-VOPO4. XANES spectra for VOPO4, LiVOPO4, and Li2VOPO4 are included as references for V5+, V4+, and V3+, respectively.

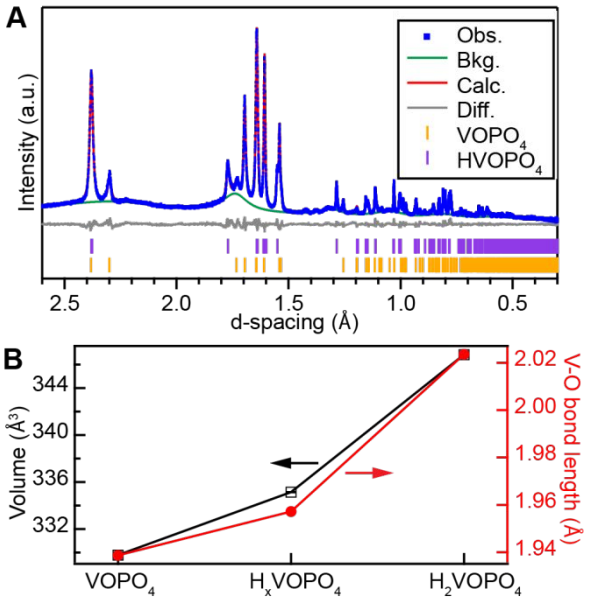

Figure 4. (A) Fitting profile for the Rietveld refinement of the HVOPO4 phase against the high-resolution synchrotron XRD pattern. (B) Refined unit cell volume and the average V-O bond length for VOPO4, HxVOPO4, and H2VOPO4. Data for H2VOPO4 are obtained from reference 28.

Synchrotron *operando* XRD was performed to interrogate the nature of the intercalation reaction during the first discharge (**Figure 5**). Upon discharge, Bragg peaks corresponding to $VOPO_4$ decrease in intensity concomitant with the emergence of a new set of peaks assigned to $HVOPO_4$ (**Figure 5A**). No peaks corresponding to LDH are observed at low angles, which is consistent with the *ex situ* XRD result in **Figure 3A**. Rietveld refinement was performed to obtain the unit cell volume (**Figure 5B**) and the scale factor (**Figure 5C**) of both the $VOPO_4$ and $HVOPO_4$ phases. The unit cell volume of $VOPO_4$ increases only from 328.32(8) $Å^3$ at the beginning of discharge to 328.97(23) $Å^3$ at the end of discharge, while the unit cell volume of $HVOPO_4$ approaches 335.5(8) $Å^3$ at the end discharge. Notably, the unit cell volume of $VOPO_4$ increases rapidly in the first 1.6 h of discharge, corresponding to the first voltage step at 1.4 V, but slowly afterward (**Figure S5**). Interestingly, this kink in the change of the unit cell volume coincides with the inception of the protonated $HVOPO_4$ phase (**Figure S5**). Therefore, the first voltage step at 1.4 V on discharge is a pseudo voltage plateau and corresponds to a single-phase reaction, where proton insertion leads to the $H_\delta VOPO_4$ ($\delta << 1$) solid solution. After 1.6 h, the scale factor for $VOPO_4$, which is proportional to its phase fraction, decreases linearly with the linear increase of the scale factor for $HVOPO_4$. Therefore the second discharge plateau at 1.25 V corresponds to a true two-phase reaction between $H_\delta VOPO_4$ and $HVOPO_4$.

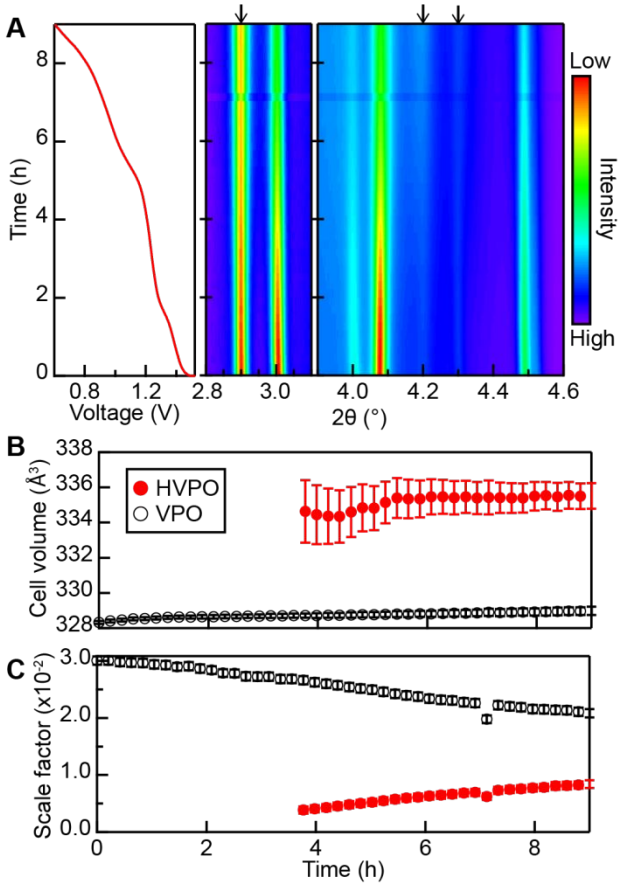

Figure 5. (A) Operando XRD patterns collected during the discharge of an ε-$VOPO_4$ cathode in an aqueous Zn ion electrolyte. Arrows indicate the positions of strong $HVOPO_4$ peaks. Refined (B) unit cell volume and (C) scale factor for both the $VOPO_4$ and $HVOPO_4$ phases.

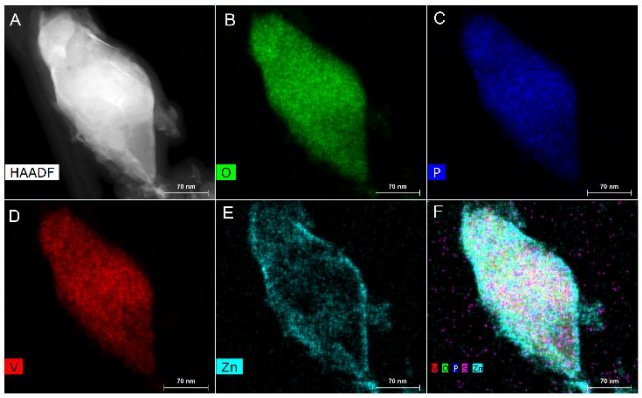

Figure 6. (A) STEM HAADF image and EDS elemental mapping of (B) O, (C) P, (D) V, (E) Zn and (F) combination of various elements measured for an ε-$VOPO_4$ particle in an electrode discharged to 0.6 V. The scale bar corresponds to 70 nm.

2.4 Fate of Zn during proton intercalation

Precipitation of Zn-based layered double hydroxide (LDH) has been recognized as the diagnostic feature of proton intercalation in AZIB due to changes in the local pH near the electrolyte.[7, 8, 11] However, the intense Bragg peaks characteristic of the crystalline LDH precipitates are not observed in either the *ex situ* high-resolution XRD or the *operando* XRD (**Figure S6**) despite the mounting evidence for proton insertion. Examination of the discharged electrode by scanning electron microscopy finds no significant changes in the morphology of the electrode after discharge (**Figure S7**). However, elemental analysis by ICP and EDS reveals a reversible change in the Zn composition after discharge and charge (**Table 1**). The ε-$VOPO_4$ electrode discharged to 0.6 V shows a Zn to P ratio of 0.42 and 0.54 by ICP and EDS analysis, respectively. In comparison, the discharge capacity is equivalent to the charge carried by only 0.31 Zn per f.u. of $VOPO_4$. Once the electrode is charged back to 1.7 V, effectively no Zn is observed by either ICP or EDS. Hence, the formation of the Zn-containing byproduct is reversible.

Table 1. Zn to P ratio measured by ICP and EDS for the electrode discharged to 0.6 V and the electrode charged to 1.7 V following a first discharge to 0.6 V.

	Discharged	Charged
Electrochemistry	0.31	0.02
ICP	0.42	0.03
EDS	0.54	0.04

To elucidate the morphology and distribution of this Zn-containing species, TEM-EDS mapping was conducted for the ε-$VOPO_4$ electrode discharged to 0.6 V. The elemental mapping of a discharged ε-$VOPO_4$ particle (**Figure 6**) shows an accumulation of Zn on the $VOPO_4$ particle surface. Similar Zn accumulation on the particle periphery is observed for two other particles (**Figure S8**).

Surface-sensitive X-ray photoelectron spectroscopy (XPS) measurement was conducted for the pristine and the cycled electrodes to interrogate the nature of the surface Zn-

containing species. The discharged electrode shows a prominent Zn 2p peak with an asymmetric shape that can be deconvoluted into two peaks (**Figure 7A**). This Zn 2p signal is attributed to the Zn formed on the particle surface as observed in the TEM (**Figure 6**C). Assignment of the Zn peaks based only on their binding energy is challenging since many surface Zn species reported for AZIBs give rise to peaks around 1022 eV (**Tables S2**).[8, 10, 29, 30] However, the absence of any S species in the XPS survey scan (**Figure S9**) rules out Zn LDH or $Zn(CF_3SO_3)_2$ as the surface Zn species. The more intense peak at 1020.8 eV disappears upon charge and is attributed to the reversible Zn-containing species formed on the $VOPO_4$ particle surface. Concurrent with the emergence of the Zn 2p peak, the O 1s spectrum (**Figure 7B)** for the discharged electrode deviates substantially from that observed for the pristine $VOPO_4$: the O 1s peak broadens and shifts to a lower binding energy compared to the pristine electrode. Since the O 1s spectrum for ε-$VOPO_4$ is expected to remain almost invariant regardless of the V oxidation state,[31] this change in the O 1s signal can only be explained by the surface Zn species. The shift to a lower binding energy is ascribed to the formation of ZnO (**Figure S10**), which has been reported to show an O 1s binding energy of 530 eV[32] and is consistent with the Zn $2p_{3/2}$ peak at 1020.8 eV. Discharging to 0.6 V also results in the appearance of a new C 1s peak at 282.5 eV (**Figure 7C)**. Such a low binding energy peak has been reported for a zinc halide/graphite composite electrode[33] and assigned to the zinc carbide C-Zn-C bond.[34] This indicates the formation of zinc carbide species in addition to oxides during the discharge process. Some ZnO likely deposits on the carbon surface, which results in the formation of Zn-C bond at the ZnO/carbon interface. Nevertheless, the exact mechanism for the zinc carbide bond formation requires further investigation and is beyond the scope of the present work. Following charging, the O 1s spectrum recovers the original shape as observed for the pristine $VOPO_4$ electrode concurrent with the disappearance of the Zn $2p_{3/2}$ peak at ~1020.8 eV and the C 1s peak at 282.5 eV. This observation is consistent with the loss of surface Zn species in the charged electrode.

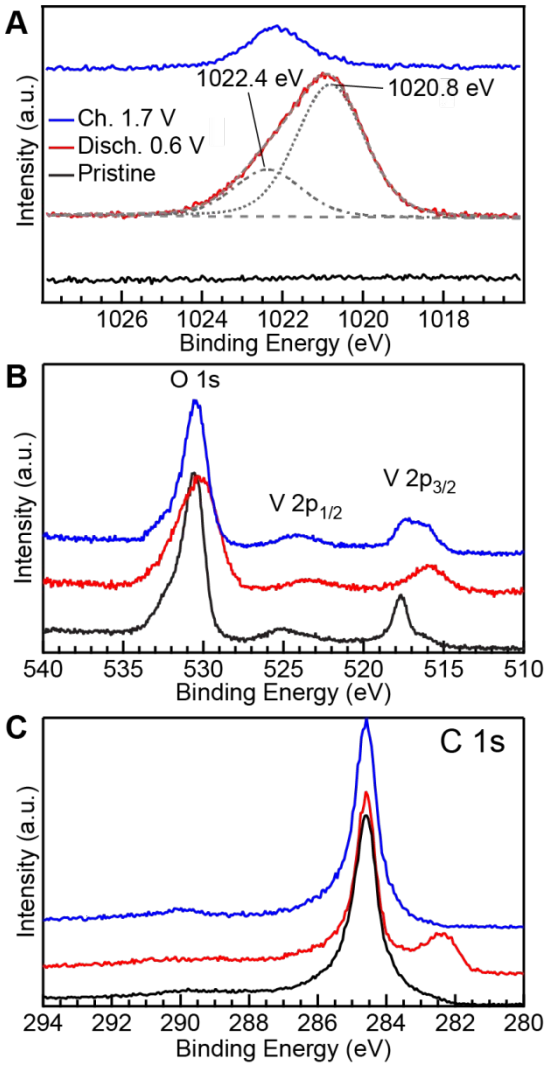

Figure 7. (A) Zn 2p, (B) O 1s and V 2p and (C) C 1s XPS core levels obtained for the pristine $VOPO_4$ electrode (black), $VOPO_4$ electrode discharged to 0.6 V (red), and $VOPO_4$ electrode charged to 1.7 V following an initial discharge to 0.6 V (blue). The dashed grey lines indicate the peak deconvolution fitting profiles.

Given the universal observation of LDH precipitates for proton intercalation in electrodes cycled in aqueous $Zn(CF_3SO_3)_2$ electrolyte,[8, 11] the formation of the ZnO coating layer presents a different reaction pathway for buffering the pH change induced by proton intercalation. The Zn-based LDH typically precipitates as isolated crystals, whereas the ZnO byproduct presents as a conformal layer that wraps around the $VOPO_4$ particles. This morphological difference suggests predominant heterogeneous nucleation for ZnO formation on ε-$VOPO_4$ particles and homogeneous nucleation for LDH in other reported electrodes. The ε-$VOPO_4$ surface could significantly lower the heterogeneous nucleation barrier for ZnO, which becomes energetically more favorable than the homogeneous nucleation of LDH.

3. Conclusions

This work reveals proton intercalation coupled with the V^{5+}/V^{4+} redox as the prevailing charge storage mechanism for the ε-$VOPO_4$ electrode cycled in an AZIB. To buffer the local pH change induced by this proton intercalation, an amorphous conformal ZnO layer is formed on the ε-$VOPO_4$ particle surface, which deviates from the established buffering mechanism through LDH formation. Such a departure highlights the important role of the electrode surface in altering the reaction pathway and byproduct to buffer the local pH change. Multimodal structural characterization is necessary to elucidate the actual reaction mechanism in future AZIBs research.

4. Experimental section

4.1 Synthesis of ε-$VOPO_4$

ε-$VOPO_4$ was synthesized through the calcination of the monoclinic H_2VOPO_4 precursor as reported by Song *et al*.[35] In a typical synthesis, 3.50 g VCl_3 (Sigma-Aldrich, 97%) and 1.76 g P_2O_5 (Sigma-Aldrich, ≥ 98%) were dissolved in 60 mL 190 proof ethanol (Pharmco-AAPER). The solution was then transferred into a 125 mL Teflon sleeve in a Parr reactor and heated at 180

℃ for 72 hours. The hydrothermal product was collected by centrifugation and washed with anhydrous ethanol three times. Subsequently, ε-$VOPO_4$ was obtained by annealing the H_2VOPO_4 precursor at 550 ℃ for 3 hours under flowing O_2 in a tube furnace. XRD measurement was conducted with a Bruker D8 diffractometer with Mo Kα radiation in the Bragg-Brentano geometry to verify the phase purity of the product.

4.2 Materials characterization

Scanning electron microscopy (SEM) images and energy-dispersive X-ray spectroscopy (EDS) were acquired with a Zesis FE-SEM Supra-55 VP scanning electron microscope.

X-ray photoelectron spectroscopy (XPS) with Al Kα X-ray radiation was used to reveal the surface chemical compositions and oxidation states of the elements in the electrodes at different states of charge.

Scanning transmission electron microscopy: High-angle annular dark-field scanning transmission electron microscopy (HAADF-STEM) imaging was performed using the FEI Talos F200X operating at 200 kV. The microscope is equipped with a four-quadrant EDS detector for elemental mapping.

High resolution synchrotron X-ray diffraction: The discharged electrode was sealed in a Kapton capillary for the high-resolution XRD at beamline 11-BM at the Advanced Photon Source (APS), Argonne National Laboratory, with a wavelength of 0.458149 Å. TOPAS Academic v6 was used for the structural analysis.[36]

X-ray absorption spectroscopy: *Ex situ* V K-edge and Zn K-edge X-ray absorption (XAS) spectra were obtained at beamline 20-BM at APS through a mail-in program. The beamline was operated with a Si (111) double-crystal monochromator. The data were collected in transmission mode and normalized using the Athena software.[37]

4.3 Electrochemical testing

Electrochemical properties of the ε-$VOPO_4$ were analyzed using pellet electrodes. The pellet electrodes were prepared by compressing a premixed ε-$VOPO_4$, acetylene black, and polyvinylidene fluoride (PVDF) powder in a weight ratio of 6:2:2 with a hydraulic press. Swagelok-type cells were assembled in air with the ε-$VOPO_4$ pellet as the cathode, Zn metal as the anode, and glass fiber as the separator. 3M $Zn(CF_3SO_3)_2$ dissolved in water was used as the electrolyte. All tests were conducted using a Bio-logic BCS 805 or a LAND battery cycler.

4.4 Synchrotron *operando* XRD measurement

Operando X-ray diffraction was conducted at beamline 17-BM at the APS with a wavelength of 0.24114 Å. Pellet electrode consisting of 60wt% ε-$VOPO_4$, 20wt% acetylene black, and 20wt% PVDF was assembled in the AMPIX cell[38] with Zn metal as the anode, glass fiber as the separator, and 3M $Zn(CF_3SO_3)_2$ in water as the electrolyte. Diffraction measurements were conducted in the transmission geometry with an area detector. The diffraction pattern was measured every 12.6 min while the cell was cycled at C/25 (1 C = 165 mAh/g) at room temperature.

Author contributions

J.W. performed the synthesis and electrochemical, SEM, and XRD characterization. H.H. performed the XPS measurement. L.Q. and G.Z. performed the TEM measurement. L.K. helped with the synthesis of $VOPO_4$ materials. J.W. and H.L. wrote the manuscript.

Conflicts of interest

The authors declare no competing financial interest.

Acknowledgements

H.L. acknowledges the financial support from the startup funding of Binghamton University and the National Science Foundation CBET-2144296. J.W. acknowledges the financial support from NYSERDA. L.Q. and G.Z. acknowledge the support from the U.S. Department of Energy (DOE), Office of Basic Energy Sciences, Division of Materials Sciences and Engineering under Award No. DE-SC0001135. The authors thank Yikang Jing for the help with elemental analysis. This research used resources of the Advanced Photon Source, a U.S. Department of Energy (DOE) Office of Science User Facility operated for the DOE Office of Science by Argonne National Laboratory under Contract No.DE-AC02-06CH11357. The Beamline 17-BM (GUP-69829) and the mail-in program of Beamline 11-BM (GUP-81365 and GUP-79646) and 20-BM (GUP-77757) contributed to the operando XRD, ex situ high-resolution XRD, and XAS data, respectively. The research also used the electron microscopy facilities of the Center for Functional Nanomaterials, which is a U.S. DOE Office of Science Facility, at Brookhaven National Laboratory under Contract No. DE-SC0012704.

Notes and references

1 D. Selvakumaran, A. Pan, S. Liang and G. Cao, *J. Mater. Chem. A*, 2019, **7**, 18209-18236.
2 T. Zhang, Y. Tang, S. Guo, X. Cao, A. Pan, G. Fang, J. Zhou and S. Liang, *Energy Environ. Sci.*, 2020, **13**, 4625-4665.
3 K. Zhu, S. Wei, H. Shou, F. Shen, S. Chen, P. Zhang, C. Wang, Y. Cao, X. Guo, M. Luo, H. Zhang, B. Ye, X. Wu, L. He and L. Song, *Nat. Commun.*, 2021, **12**, 6878.
4 Y. Wu, Z. Zhu, Y. Li, D. Shen, L. Chen, T. Kang, X. Lin, Z. Tong, H. Wang and C. S. Lee, *Small*, 2021, **17**, e2008182.
5 K. Zhu, T. Wu and K. Huang, *Energy Storage Mater.*, 2021, **38**, 473-481.
6 Y. Yuan, R. Sharpe, K. He, C. Li, M. T. Saray, T. Liu, W. Yao, M. Cheng, H. Jin, S. Wang, K. Amine, R. Shahbazian-Yassar, M. S. Islam and J. Lu, *Nat. Sustain.*, 2022, **5**, 890-898.
7 P. Oberholzer, E. Tervoort, A. Bouzid, A. Pasquarello and D. Kundu, *ACS Appl. Mater. Interfaces*, 2019, **11**, 674-682.
8 X. Liu, H. Euchner, M. Zarrabeitia, X. Gao, G. A. Elia, A. Groß and S. Passerini, *ACS Energy Lett.*, 2020, **5**, 2979-2986.
9 F. Wang, L. E. Blanc, Q. Li, A. Faraone, X. Ji, H. H. Chen-Mayer, R. L. Paul, J. A. Dura, E. Hu, K. Xu, L. F. Nazar and C. Wang, *Adv. Energy Mater.*, 2021, **11**, 2102016.
10 C. Li, R. Kingsbury, A. S. Thind, A. Shyamsunder, T. T. Fister, R. F. Klie, K. A. Persson and L. F. Nazar, *Nat. Commun.*, 2023, **14**, 3067.

11 C. Li, R. Kingsbury, L. Zhou, A. Shyamsunder, K. A. Persson and L. F. Nazar, *ACS Energy Lett.*, 2022, DOI: 10.1021/acsenergylett.1c02514, 533-540.
12 G. Li, Z. Yang, Y. Jiang, C. Jin, W. Huang, X. Ding and Y. Huang, *Nano Energy*, 2016, **25**, 211-217.
13 X. Chen, H. Zhang, J.-H. Liu, Y. Gao, X. Cao, C. Zhan, Y. Wang, S. Wang, S.-L. Chou, S.-X. Dou and D. Cao, *Energy Storage Mater.*, 2022, **50**, 21-46.
14 S. Linghu, J. Ye, K. Deng, P. Liu, Y. Zhong, T. You, W. Tian and J. Ji, *J. Power Sources*, 2024, **592**, 233922.
15 M. Liao, Y. Cao, Z. Li, J. Xu, Y. Qi, Y. Xie, Y. Peng, Y. Wang, F. Wang and Y. Xia, *Angew. Chem. Int. Ed. Engl.*, 2022, **61**, e202206635.
16 D. Zhao, X. Pu, S. Tang, M. Ding, Y. Zeng, Y. Cao and Z. Chen, *Chem. Sci.* , 2023, **14**, 8206-8213.
17 L. Cao, D. Li, T. Pollard, T. Deng, B. Zhang, C. Yang, L. Chen, J. Vatamanu, E. Hu, M. J. Hourwitz, L. Ma, M. Ding, Q. Li, S. Hou, K. Gaskell, J. T. Fourkas, X. Q. Yang, K. Xu, O. Borodin and C. Wang, *Nat. Nanotech.*, 2021, **16**, 902-910.
18 F. Wang, W. Sun, Z. Shadike, E. Hu, X. Ji, T. Gao, X. Q. Yang, K. Xu and C. Wang, *Angewandte Chemie*, 2018, **57**, 11978-11981.
19 J. Wang, K. Lee, M. S. Whittingham and H. Liu, *Chemistry of Materials*, 2023, **35**, 9399-9411.
20 C. Siu, I. D. Seymour, S. Britto, H. Zhang, J. Rana, J. Feng, F. O. Omenya, H. Zhou, N. A. Chernova, G. Zhou, C. P. Grey, L. F. J. Piper and M. S. Whittingham, *Chem. Commun.*, 2018, **54**, 7802-7805.
21 T. R. F. Girgsdies, R. Schlögl, W.-S. Dong, J.K. Bartley, G.J. Hutchings *Solid State Sci.*, 2006, **8**, 807-812.
22 Z. Chen, Q. Chen, L. Chen, R. Zhang, H. Zhou, N. A. Chernova and M. S. Whittingham, *J. Electrochem. Soc.*, 2013, **160**, A1777-A1780.
23 P. Hu, T. Zhu, X. Wang, X. Zhou, X. Wei, X. Yao, W. Luo, C. Shi, K. A. Owusu, L. Zhou and L. Mai, *Nano Energy*, 2019, **58**, 492-498.
24 J. S. Ko, P. P. Paul, G. Wan, N. Seitzman, R. H. DeBlock, B. S. Dunn, M. F. Toney and J. Nelson Weker, *Chem. Mater.*, 2020, **32**, 3028-3035.
25 J. Rana, Y. Shi, M. J. Zuba, K. M. Wiaderek, J. Feng, H. Zhou, J. Ding, T. Wu, G. Cibin, M. Balasubramanian, F. Omenya, N. A. Chernova, K. W. Chapman, M. S. Whittingham and L. F. J. Piper, *J. Mater. Chem. A*, 2018, **6**, 20669-20677.
26 B. Wen, Q. Wang, Y. Lin, N. A. Chernova, K. Karki, Y. Chung, F. Omenya, S. Sallis, L. F. J. Piper, S. P. Ong and M. S. Whittingham, *Chem. Mater.*, 2016, **28**, 3159-3170.
27 E. Chalmin, F. Farges and G. E. Brown, *Contrib. Mineral. Petrol.* , 2008, **157**, 111-126.
28 W. T. A. H. J.T. Vaughey, and Allan J. Jacobson*, *Inorg. Chem.*, 1994, **33**, 2481-2487.
29 K. Zhu, T. Wu and K. Huang, *Chem. Mater.*, 2021, **33**, 4089-4098.
30 C. Lee, Y. Hong, D. Kim, Y. Lim, J. W. Choi and S.-Y. Chung, *Adv. Funct. Mater.*, 2023, **33**, 2303763.
31 N. F. Quackenbush, L. Wangoh, D. O. Scanlon, R. Zhang, Y. Chung, Z. Chen, B. Wen, Y. Lin, J. C. Woicik, N. A. Chernova, S. P. Ong, M. S. Whittingham and L. F. J. Piper, *Chem. Mater.*, 2015, **27**, 8211-8219.
32 J. Duchoslav, R. Steinberger, M. Arndt and D. Stifter, *Corros. Sci.*, 2014, **82**, 356-361.
33 A. Ejigu, L. W. Le Fevre and R. A. W. Dryfe, *ACS Appl. Mater. Interfaces*, 2021, **13**, 14112-14121.
34 J. J. Beltran, C. A. Barrero and A. Punnoose, *Phys. Chem. Chem. Phys.*, 2019, **21**, 8808-8819.
35 Y. Song, P. Y. Zavalij and M. S. Whittingham, *J. Electrochem. Soc.*, 2005, **152**, A721.
36 A. A. Coelho, *J. Appl. Cryst.*, 2018, **51**, 210-218.
37 B. Ravel and M. Newville, *J. Synchrotron Radiat.*, 2005, **12**, 537-541.
38 O. J. Borkiewicz, B. Shyam, K. M. Wiaderek, C. Kurtz, P. J. Chupas and K. W. Chapman, *J. Appl. Cryst.*, 2012, **45**, 1261-1269.

The data supporting this article have been included as part of the Supplementary Information. Raw data were generated at Binghamton University and Brookhaven National Laboratory and are available from the corresponding author upon request.